



Developing high-performance oxygen electrodes for intermediate solid oxide cells (SOC) prepared by $\text{Ce}_{0.8}\text{Gd}_{0.2}\text{O}_{2-\delta}$ backbone infiltration

Ömer Faruk Aksoy¹ · Bartłomiej Lemieszek² · Murat Murutoğlu¹ · Jakub Karczewski³ · Piotr Jasiński² · Sebastian Molin²

Received: 4 July 2024 / Accepted: 25 September 2024 / Published online: 7 October 2024
© The Author(s) 2024

Abstract

$\text{Gd}_{0.2}\text{Ce}_{0.8}\text{O}_{2-\delta}$ (GDC) porous backbone infiltration with $\text{La}_{0.6}\text{Sr}_{0.4}\text{CoO}_{3-\delta}$ (LSC), PrOx and LSC: PrOx as a composite oxygen electrode for intermediate solid oxide cells are conducted within the scope of this work. Samples were characterized using scanning electron microscopy (SEM), energy dispersive X-ray spectroscopy (EDX), and electrochemical impedance spectroscopy (EIS). A uniform distribution of the infiltrated material inside the backbone and at the electrolyte-backbone interface was achieved. EIS measurements on the prepared symmetrical samples showed electrode polarization resistance (R_p) values of $0.029 \Omega\cdot\text{cm}^2$, $0.23 \Omega\cdot\text{cm}^2$, and $0.44 \Omega\cdot\text{cm}^2$ for LSC, LSC: PrOx, and PrOx at 600°C , respectively. Long-term stability measurements at 600°C for 100 h showed a slight increase in polarization resistance during the measurement period. Fuel cell measurements of commercial cells (Elcogen) with porous oxygen electrode consisting of GDC infiltrated with LSC showed an increase in power density compared to the reference cell with a value of $0.53 \text{ W}\cdot\text{cm}^{-2}$ obtained at 600°C . It is proven that infiltration via polymeric precursor into porous scaffolds as backbone oxygen electrode layer is effective and convenient method to develop high performance and stable solid oxide cells.

Keywords Solid oxide cells · Oxygen electrode · Infiltration · LSC · Praseodymium oxide

1 Introduction

Solid oxide cells (SOCs) are one of the promising technologies that are a potentially important part of energy transformation [1]. Typically, SOC can operate in two modes: fuel cell - solid oxide fuel cell (SOFC) and electrolyzer - solid oxide electrolysis cell (SOEC) [2].

Originally, SOC operated at temperatures above 1000°C , and it immediately became obvious that to implement the technology, a significant reduction in the system's operating temperature was needed. The current objective is to provide efficient cells operating in the

intermediate temperature range to reduce cost significantly [3, 4]. To achieve this goal, improvements in oxygen electrode development must take place. The reason for this is the polarization resistance of this electrode, which is responsible for a significant part of the resistance of the entire cell [5]. Therefore, in recent years, there has been an intensification of research on effective materials for oxygen electrodes operating at low temperatures. Among the analyzed materials, mixed ionic-electronic conductors (MIECs) have gained popularity, as the oxygen reduction reaction takes place at triple phase boundaries where both the presence of electrons and the transport of ions in the material are possible [6]. The materials analyzed for use as an oxygen electrode in cells include perovskite oxides such as $\text{La}_{1-x}\text{Sr}_x\text{MnO}_{3-\delta}$ (LSM) [7, 8], $\text{La}_{1-x}\text{Sr}_x\text{CoO}_{3-\delta}$ (LSC) [6, 9–13], or $\text{La}_{1-x}\text{Sr}_x\text{Co}_{1-y}\text{Fe}_y\text{O}_{3-\delta}$ (LSCF) [14–17]. Additionally, materials such as PrOx and Ruddlesden-Popper phase $\text{Pr}_2\text{NiO}_{4+\delta}$ are currently gaining popularity [18, 19].

The efficiency of the oxygen electrode is also influenced by its manufacturing technique. The most popular techniques used to prepare these electrodes include screen-printing [20], tape-casting [21–24], spin-coating [25–27],

¹ Department of Material Science and Engineering, Gebze Technical University, Kocaeli 41400, Turkey

² Advanced Materials Centre, Faculty of Electronics, Telecommunications and Informatics, Gdańsk University of Technology, ul. G. Narutowicza 11/12, Gdańsk 80-233, Poland

³ Advanced Materials Centre, Faculty of Applied Physics and Mathematics, Gdańsk University of Technology, ul. G. Narutowicza 11/12, Gdańsk 80-233, Poland

dip-coating [28], and more advanced techniques such as pulsed laser deposition (PLD) [29], atomic layer deposition (ALD) [30, 31], spray pyrolysis [6, 10], or chemical vapor deposition (CVD) [32]. Furthermore, the infiltration technique is increasingly used, in which a porous backbone made of an electrolyte material with high ionic conductivity is impregnated with a material with high electronic conductivity [33–36].

For example, in the work of Choi et al., described the infiltration of $\text{La}_{n+1}\text{Ni}_n\text{O}_{3n+1}$ material ($n=1,2,3$) into the porous structure of YSZ (yttria-stabilized zirconia). A porous backbone with a thickness of about 50 μm was infiltrated with the prepared precursor until the loading reached 45 wt%, then the prepared oxygen electrode was annealed at 850 °C. Electrochemical Impedance Spectroscopy (EIS) measurements showed polarization resistance values of 0.120 $\Omega\cdot\text{cm}^2$ for La_2NiO_4 , 0.112 $\Omega\cdot\text{cm}^2$ for $\text{La}_3\text{Ni}_2\text{O}_7$, and 0.068 $\Omega\cdot\text{cm}^2$ for $\text{La}_4\text{Ni}_3\text{O}_{10}$ at a temperature of 750 °C. The full cell measurements, with the $\text{La}_4\text{Ni}_3\text{O}_{10}$ as an oxygen electrode, reached 0.889 $\text{W}\cdot\text{cm}^{-2}$ at 750 °C [37]. Shah et al. described the infiltration of $\text{La}_{0.6}\text{Sr}_{0.4}\text{Co}_{0.2}\text{Fe}_{0.8}\text{O}_{3-\delta}$ into porous GDC (gadolinium-doped ceria). It has been shown that the optimal sintering temperature for GDC backbone is between 1100 °C and 1200 °C. Loading of 12.5 wt%, of material into the porous backbone showed the lowest polarization resistance (R_p) equal to 0.24 $\Omega\cdot\text{cm}^2$ at a temperature of 600 °C [38]. Huang et al. described the infiltration of the porous YSZ backbone with LSM ($\text{La}_{0.8}\text{Sr}_{0.2}\text{MnO}_{3-\delta}$) material as a potential oxygen electrode. All tested combinations showed similar catalytic properties, and the polarization resistance values were approximately 0.4 $\Omega\cdot\text{cm}^2$ at 700 °C [39]. Cheng et al. described the process of infiltration of the composite YSZ: $\text{La}_{0.8}\text{Sr}_{0.2}\text{FeO}_{3-\delta}$ (1:1 ratio) with LSCF ($\text{La}_{0.6}\text{Sr}_{0.4}\text{Co}_{0.2}\text{Fe}_{0.8}\text{O}_{3-\delta}$) material. With only two infiltration cycles of LSCF, decrease in polarization resistance from 1.4 $\Omega\cdot\text{cm}^2$ (for sample without infiltration) to 0.16 $\Omega\cdot\text{cm}^2$ at a temperature of 700 °C, was observed. The prepared cell with the proposed oxygen electrode showed a power density of 0.4 $\text{W}\cdot\text{cm}^{-2}$ at 700 °C [40]. Samson et al. described the infiltration of a porous $\text{Ce}_{0.9}\text{Gd}_{0.1}\text{O}_{2-\delta}$ backbone with a thickness of approximately 25 μm with LSC as a potential oxygen electrode for intermediate-temperature solid oxide fuel cells. It was found that for a precursor solution with a concentration of approximately 1 M, the optimal number of infiltration cycles was 9. It was also shown that the optimal annealing temperature was set at 600 °C. The polarization resistance of the obtained oxygen electrode at 600 °C was 0.044 $\Omega\cdot\text{cm}^2$ [34]. Nicollet et al. proposed infiltration porous GDC with Pr_6O_{11} material. It has been shown that the optimal backbone thickness was determined as 14 μm . Infiltration with the Pr_6O_{11} precursor continued until a loading of 30 wt% was achieved (3–4 cycles). After the preparation

process, the samples were annealed at 600 °C. EIS measurements showed a very low value of polarization resistance, equal to 0.028 $\Omega\cdot\text{cm}^2$ at the same temperature. The cell with the described oxygen electrode showed a power density of 0.825 $\text{W}\cdot\text{cm}^{-2}$ at 600 °C compared to about 0.4 $\text{W}\cdot\text{cm}^{-2}$ for a commercial cell [18].

In this work investigation on the process of infiltration of a porous GDC (gadolinium-doped ceria) backbone with materials such as LSC, PrOx, and the LSC: PrOx composite were described. The infiltration process allows for the steady distribution of nanoparticles of the impregnated material throughout the structure of the backbone material. Electrochemical activity measurements showed very good oxygen reduction reaction (ORR) properties of the materials. Among the three materials discussed, LSC turned out to be the most promising. The use of the best combination as the oxygen electrode in the solid oxide fuel cell showed an increase in power density of the infiltrated commercial Elcogen cell compared to the plain Elcogen cell as reference sample which is denoted as EL throughout the paper.

2 Experimental

In this work, infiltration of porous air electrodes made of $\text{Ce}_{0.8}\text{Gd}_{0.2}\text{O}_{2-\delta}$ (GDC) backbone with $\text{La}_{0.6}\text{Sr}_{0.4}\text{CoO}_{3-\delta}$ (LSC), PrOx and LSC: PrOx (1:1 by precursor vol.) were performed. Various characterization techniques have been done, such as Electrochemical Impedance Spectroscopy (EIS), Scanning Electron Microscopy with Energy Dispersive X-ray Spectroscopy (SEM-EDS) and X-ray diffraction (XRD).

2.1 Sample preparation

Polymeric precursors for infiltration were prepared with the Pechini method [41]. Nitrate salts in the form of $\text{La}(\text{NO}_3)_3\cdot 6\text{H}_2\text{O}$ (purity 99.9%, Alfa Aesar), $\text{Sr}(\text{NO}_3)_2$ (purity 99%, Sigma Aldrich), $\text{Co}(\text{NO}_3)_3\cdot 6\text{H}_2\text{O}$ (purity 99%, Sigma Aldrich), or $\text{Pr}(\text{NO}_3)_3\cdot 6\text{H}_2\text{O}$ (99.9% of purity, Alfa Aesar) were dissolved in the appropriate stoichiometry in distilled water with a total molar concentration of 0.2 M (or nitrates as 0.04 M of ethylene glycol). Ethylene glycol was then added to perform the polymerization process with heating at 80 °C on a hotplate with continuous stirring. Heating was continued until all the water had evaporated from the solution. The completion of this process was determined by the decrease in the mass of the solution by the mass of water measured at the initial stage.

0.8 g of commercially available GDC powder (GDC-20 K, Daiichi Kigenso Kagaku Kogyo, Japan) was placed in a mould with a diameter of 16 mm and pressed at 98 MPa

for 1 min. Sintering was carried out at 1400 °C for 10 h to obtain a dense structure. After sintering, the pellets shrank to an average diameter of 13 mm with a thickness of around 0.6 mm.

The next step was preparation a porous backbone with a porosity of approximately 50%. Prepared slurry, for wet-powder spraying, consisting of toluene, ethanol, (with ratio toluene to ethanol 1:4) binder (Heraeus) and GDC powder (3 wt%), sprayed using an airbrush (Paasche VLS) onto GDC pellets on a hot plate heated to 250 °C. The slurry was kept in an ultrasonic bath for homogenization before spraying. As a result of contact with the hot surface, the solvents evaporated instantaneously, leaving the scaffold structure. Porous backbone was prepared on both sides of the dense GDC pellets. After spraying, sintering was carried out, at a temperature of 1150 °C for 2 h in order to obtain adequate mechanical properties and a good connection between the dense electrolyte surface and the backbone. Prepared pellets with a porous backbone were used for infiltration. Wet-powder spraying and post-sintering infiltration are graphically shown in Fig. 1.

The infiltration process was carried out by immersing pellets with a porous backbone into the prepared precursor solution (1 ml) and then removing the air remaining from the pores using a vacuum chamber (0.08 Pa) for 10 min. Excess solution was then gently removed with a paper towel. The utilization of the immersion technique permitted the simultaneous and uniform application of the precursor solution to both sides of the sample. The samples prepared in this way were then pre-annealed on a hotplate at a temperature of 400 °C. The pre-annealing process took place in 3 stages: 90 °C–15 min, 180 °C–15 min and 400 °C–15 min. The optimum loading volume of the porous material with the impregnated material was determined using electrochemical impedance spectroscopy (EIS). It was found that the lowest values of the polarization resistance were obtained for the samples that were infiltrated for 6 cycles. After completing the procedure, the samples were annealed in a muffle

furnace (Carbolyte RHF 16/8 box furnace) at 600 °C for 2 h. The samples prepared in this way were used for further research.

2.2 Characterization

Electrochemical impedance spectroscopy (EIS) measurements were conducted on the prepared symmetrical cells, to evaluate the ohmic and polarization resistance (R_{ohm} and R_p). An LSC paste (Fiaxell) current collector layer was applied to both side of the pellets and annealed at 600 °C for two hours. The samples were placed in a compression cell where the electrical contact was a gold mesh connected to platinum wires on both sides of the sample. These wires were led outside the furnace where they were connected to the Novocontrol Alpha-A potentiostat, which was used to perform the measurements. For EIS measurements, an excitation amplitude of 25 mV and in frequency range of 3 MHz to 50 MHz were used. Measurements were performed in the temperature range from 600 °C to 300 °C, every 50 °C in the range of 600 °C–400 °C, and every 25 °C in the range of 400 °C–300 °C. An atmosphere of synthetic air was used with a controlled flow of 50 ml min⁻¹.

SEM-EDS analysis of fractures, with appropriate materials was performed using a field emission scanning electron microscope (FEI Quanta FEG250) equipped with a secondary ET detector. The accelerating voltage was maintained at 10 keV.

Commercial half-cells (ASC-400B, Elcogen), comprising a NiO-YSZ (fuel electrode), YSZ/GDC (electrolyte), without an oxygen electrode, were used for the full cell measurements. Infiltrated samples were labeled as EL-9 C-LSC and EL-12 C-LSC respectively depending on their infiltration cycle as 9 or 12 times. The porous backbone was prepared in the same procedure as for symmetrical measurements. The infiltration process was conducted by applying the precursor to the surface of the porous GDC and subjecting it to pre-annealing at 400 °C on a hot plate. Once the

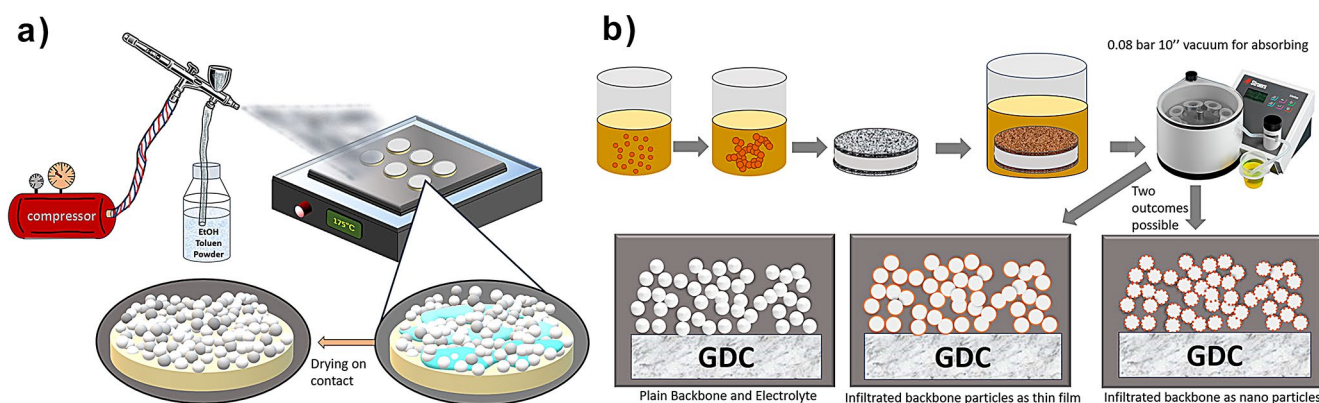


Fig. 1 Graphical representation of **a)** GDC backbone spraying on to GDC pellets and **b)** infiltration of porous GDC backbones with solutions

optimal loading of the GDC backbone had been achieved, the samples were annealed at 600 °C for two hours. The reference sample was a commercial full cell (Elcogen) with an LSC oxygen electrode.

The fuel cell characterization was performed using an Open Flanges V5 test setup (Fiaxell Sàrl Technologies). The prepared cell was electrically connected on the fuel side by a nickel foam and on the air side by a gold mesh. The cell was placed in a Kittec furnace equipped with a PID temperature controller. The wires were connected to a Solartron 1260/1287 frequency analyzer for impedance and current-voltage characterization. The cell was heated to 600 °C and held isothermally. The fuel electrode was reduced in dry hydrogen gas (100 ml min^{-1}), which was supplied as fuel, while synthetic air was delivered to the oxygen electrode as the oxidant (200 ml min^{-1}). To characterize the cell, impedance spectra were measured at open-circuit voltage (OCV) conditions in the frequency range of 100 kHz–0.1 Hz. For evaluating the cell performance, current-voltage characteristics were performed.

3 Results and discussion

3.1 Sample preparation

Following the infiltration process, the prepared samples were subjected to SEM-EDX analysis to confirm the uniform distribution of the infiltrated material within the backbone structure. The SEM images in Fig. 2 show the fractures of the samples after infiltration for LSC, LSC: PrOx, and PrOx. The backbone structure is well formed, despite the presence of heterogeneities, segregation and flake structure, and the pore size is relatively small. Nevertheless, the presence of nanoparticles derived from the respective materials was discerned in all three infiltrated precursors (LSC, PrOx and LSC: PrOx) (red circles). Concurrently, the loading level is relatively low.

An EDX analysis was conducted to ascertain the distribution of materials within the porous backbone. Spot EDX analysis was performed on the fractures of samples immersed in LSC, LSC: PrOx and PrOx alone. Figure 3 shows the distribution of measurement spots. Figure 4 shows EDX spectra with elements identified at point 4, closest to the electrolyte. The elements expected to be introduced into the backbone by the immersion technique were identified.

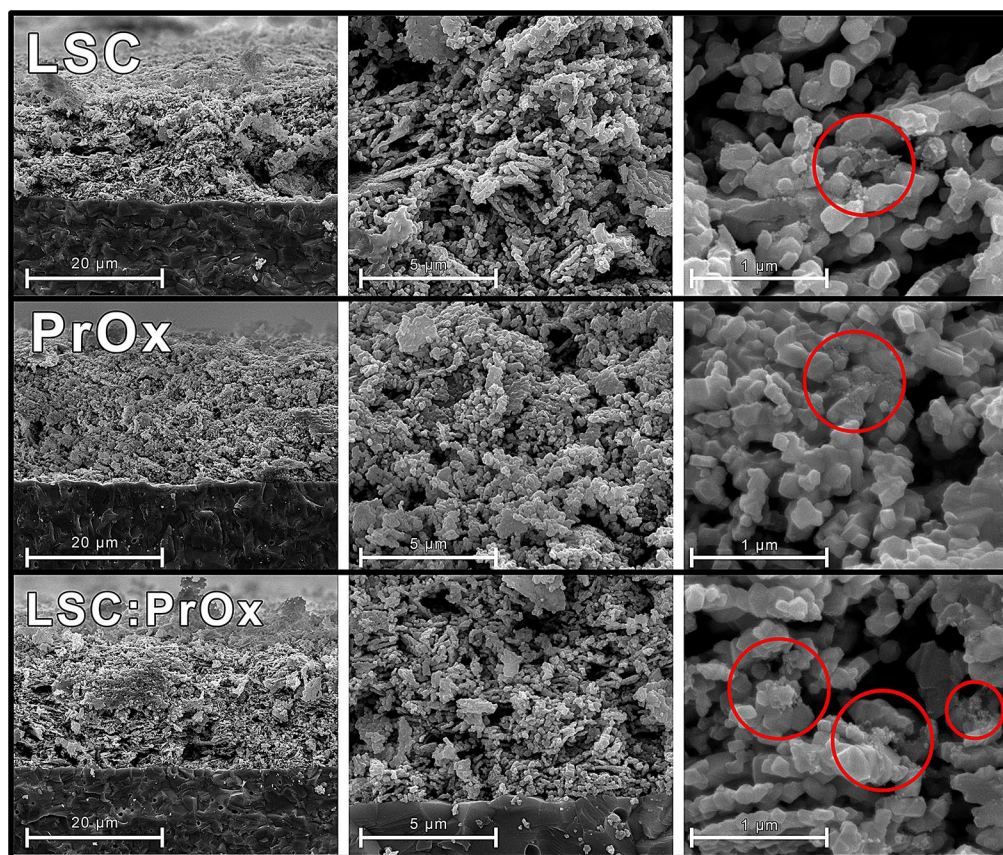


Fig. 2 SEM images of LSC, LSC: PrOx and PrOx infiltrated backbones

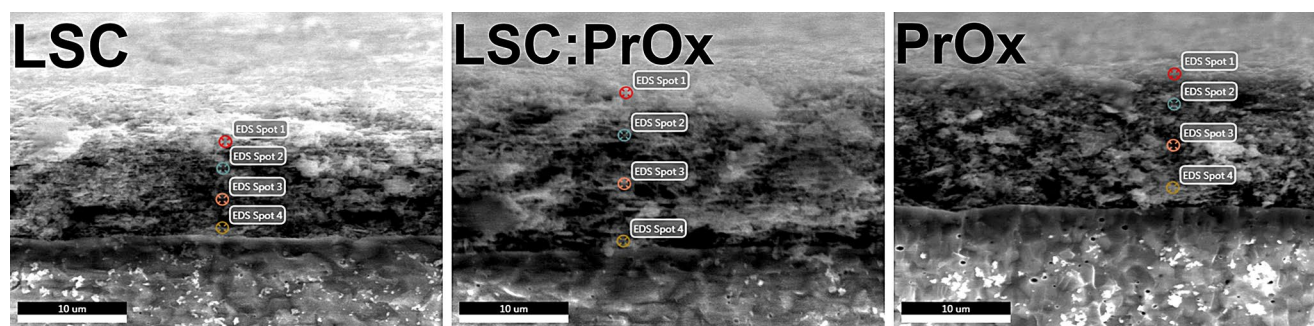


Fig. 3 Location spots of EDX responses from infiltrated symmetrical cells in the backbone

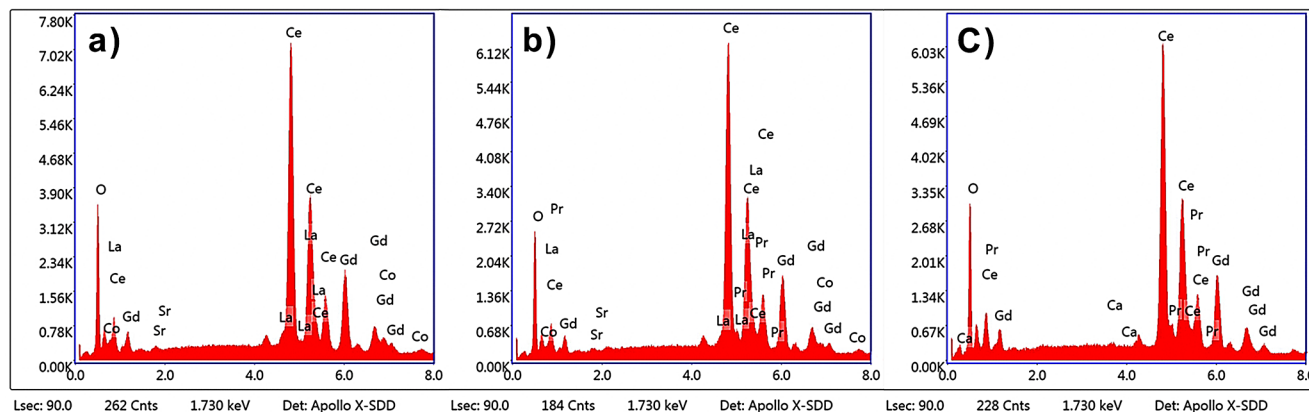


Fig. 4 EDX analysis of a) LSC, b) LSC: PrOx and c) PrOx infiltrated backbones at spot 4

Table 1 presents the atomic concentration of identified cations obtained at each of the analysed points. Moreover, no segregation of strontium or other elements was identified, and the atomic distribution was found to be consistent with the expected pattern. Furthermore, a markedly higher loading of LSC in comparison to PrOx was discerned. This result was unexpected, given that the total cation concentration was identical in both precursors. The LSC was responsible for approximately 14% of the total signal, while PrOx accounted for approximately 4.5%. In the case of the composite-infiltrated sample, the signal ratio of LSC to PrOx was, on average, 3:1 at points 2, 3, and 4. However, at point 1, the ratio was higher, amounting to 5.4:1.

The EDX analysis performed was mainly for qualitative analysis, i.e. to demonstrate the presence of specific elements in the porous GDC backbone and for rough comparison of values. This was due to the high quantitative inaccuracy of EDX for atomic concentrations below 5%. An effective and uniform distribution of the impregnated materials in the porous GDC backbone was demonstrated by SEM-EDX analysis.

3.2 Electrochemical impedance spectroscopy

A series of measurements were conducted using electrochemical impedance spectroscopy on symmetrical samples with an electrode layer on either side of the electrolyte. The objective was to determine the electrochemical performance of the proposed oxygen electrode.

Figure 5a and b show the area specific resistance (ASR) dependence as a function of temperature for three types of samples, including ohmic resistance and electrode polarization.

The analysis demonstrated that the lowest ohmic resistance values were observed in samples infiltrated with an LSC: PrOx composite, followed by samples infiltrated with LSC. Conversely, the highest ohmic resistance values were observed in samples that had been infiltrated with PrOx alone. The activation energy values (E_a) were also determined for the aforementioned data set. Furthermore, the lowest activation energy at higher temperatures was identified for samples infiltrated in PrOx. Similar E_a values were obtained at lower temperatures for all three tested types of specimens.

In terms of polarization resistance, the LSC-infiltrated sample obtain the lowest polarization resistance at a temperature of 600 °C, followed by the GDC-LSC: PrOx-infiltrated

Table 1 EDX output as atomic percentage values of all samples

Spot number	LSC				LSC: PrOx				PrOx			
	1	2	3	4	1	2	3	4	1	2	3	4
La L	3.53	4.09	4.30	3.44	1.78	2.05	1.61	2.87	-	-	-	-
Sr L	4.03	3.88	4.16	4.30	5.96	2.44	3.11	1.77	-	-	-	-
Co L	6.69	7.04	6.82	5.66	3.19	3.81	3.25	3.58	-	-	-	-
Ce L	68.93	68.22	68.00	69.12	69.90	71.68	72.38	71.44	77.76	77.42	76.24	76.32
Gd K	16.81	16.78	16.72	17.49	17.13	16.87	17.08	17.50	19.11	18.31	18.13	18.65
Pr L	-	-	-	-	2.04	3.15	2.58	2.83	3.13	4.27	5.63	5.03

sample, and the GDC-infiltrated PrOx-infiltrated sample had the highest values. The polarization resistance for the oxygen electrode in the form of porous GDC immersed in LSC was $0.029 \Omega \cdot \text{cm}^2$, $0.68 \Omega \cdot \text{cm}^2$ and $7.89 \Omega \cdot \text{cm}^2$ at temperatures of 600°C , 500°C and 400°C respectively. In the case of the LSC: PrOx sample, it was $0.23 \Omega \cdot \text{cm}^2$, $0.93 \Omega \cdot \text{cm}^2$ and $9.75 \Omega \cdot \text{cm}^2$, respectively, and for the samples with GDC backbone infiltrated in PrOx alone, it was $0.42 \Omega \cdot \text{cm}^2$, $2.95 \Omega \cdot \text{cm}^2$ and $17.38 \Omega \cdot \text{cm}^2$, respectively, at the same temperatures. Significant differences in activation energy at higher temperatures was noticeable. The sample infiltrated with the LSC: PrOx composite has a significantly lower E_a value than the others. This outcome is likely attributable to the combination of the properties of the two materials. It is also noteworthy that the E_a value of 1.523 eV for LSC in the temperature range between 600°C and 450°C is considerably higher than the data presented in the literature, for example, the value of 1.099 eV reported in the study conducted by Samson A. et al. [42]. At lower temperatures it was noticeable that the E_a for LSC and LSC: PrOx are almost identical. This was most likely due to the high electrical conductivity of LSC compared to PrOx, which dominates over praseodymium oxide at lower temperatures in the composite. The significantly higher value of polarization resistance for PrOx was the result of the low electrical conductivity of the material at low temperatures [43]. Figure 6 shows the Nyquist plots obtain for the samples tested at different temperatures. The ohmic resistance part has been subtracted to compare the electrode performance only. At 600°C , high frequencies are related to charge transfer and transport of oxide ions through the composite to the electrolyte interface in TPB (triple-phase boundary), medium frequencies are related to diffusion of adsorbed oxygen and finally low frequencies were related to the oxygen reduction reaction (conversion). Two different impedance semicircles were observed at 400°C and 500°C . The semicircle in higher frequencies was related to the grain boundary polarization and the semicircle in lower frequencies was related to the oxygen electrode polarization mentioned above. The polarization value of the oxygen electrode (hereafter referred to as R_p) was the diameter of the semi-circle on the real impedance axis, multiplied by the area of the active electrode surface and divided by two to obtain the ASR of one side of the electrode, due to the symmetrical nature of the samples tested.

3.3 Long-term stability

Figure 7a illustrates the EIS spectra recalculated to the active area of the oxygen electrode. Figure 7b depicts the change in ohmic resistance calculated throughout the experiment, while Fig. 7c illustrates the change in polarization

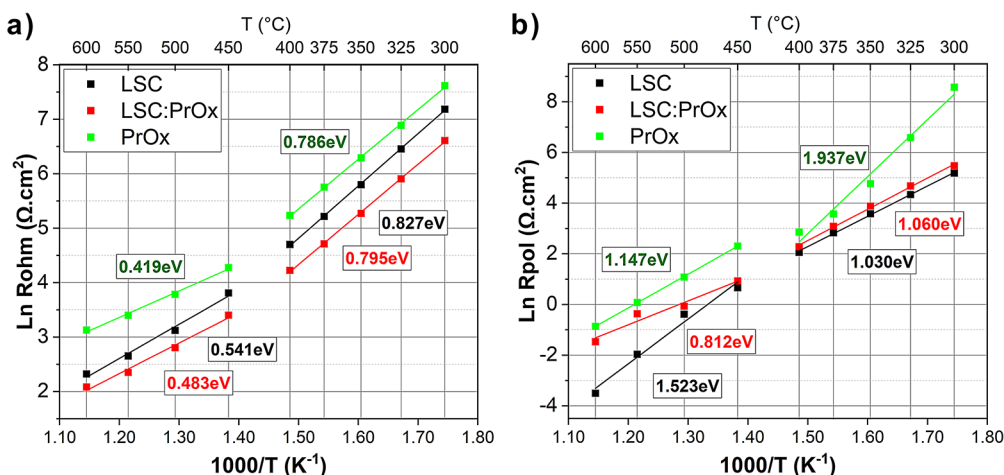


Fig. 5 ASR vs. temperature plots of infiltrated symmetrical cells as a) R_{ohm} and b) R_p with calculated activation energy

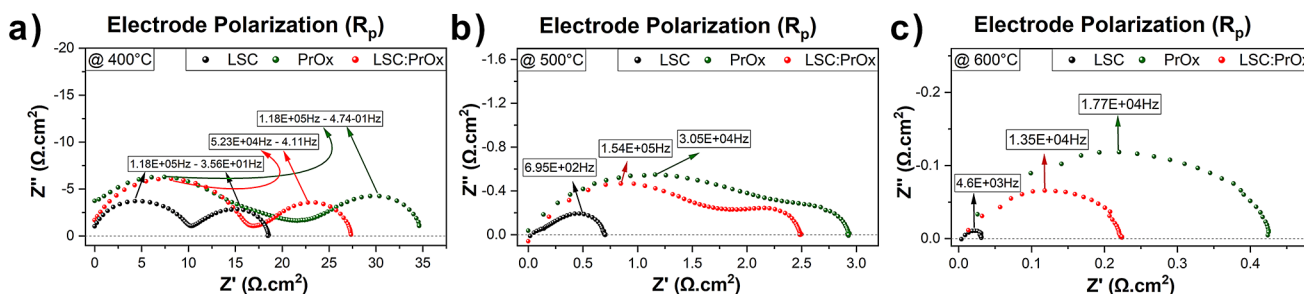


Fig. 6 Nyquist plots of infiltrated symmetrical cells at a) 400 °C, b) 500 °C and c) 600 °C

resistance. The initial decline was followed by a period of stabilisation, which commenced after 30 h. The initial R_{ohm} value was determined to be $10.58 \Omega \cdot \text{cm}^2$, and after 50 h of the experiment, a decrease of approximately $0.19 \Omega \cdot \text{cm}^2$ was observed. Between 50 and 100 h, a slight increase in ohmic resistance was noted, amounting to $0.005 \Omega \cdot \text{cm}^2$. The reduction in R_{ohm} observed during the experiment may be attributed to minor microstructural alterations at the LSC-GDC interphase, including alterations in porosity, grain size of the LSC nanoparticles, and the number and length of TPBs. The electrode polarization resistance exhibited an increase from an initial value of $0.0375 \Omega \cdot \text{cm}^2$ to $0.0464 \Omega \cdot \text{cm}^2$, representing a 24% change in ΔASR after 100 h in LSC. This phenomenon is a common occurrence in literature, with a threefold increase in polarization resistance achieved when screen-printed and deposited films are used in comparison to the conventional methods described in literature [47, 48]. The observed increase in R_p with the passage of time is attributed to grain coarsening, which was a consequence of a reduction in the electronically active areas and length of TPB.

3.4 Fuel cell testing

Analysis of the oxygen electrode in the form of symmetrical measurements using electrochemical impedance spectroscopy gives a general overview of the material's properties. For a more comprehensive characterization, measurements were performed on full cells. The described combination of a porous GDC backbone infiltrated with LSC was used as the oxygen electrode. Porous GDC backbone on commercially available half cells was prepared in the same procedure as symmetrical cells and infiltrated with the LSC precursor. In this case it was necessary to change the method from immersing to dropping due to the nature of the samples. It was found that this method gave similar results after 12 infiltration cycles. The reference was a commercial cell with an oxygen electrode in the form of LSC. Figure 8a and b, show the I-V curves and Fig. 8c and d EIS graphs obtained for cells with the proposed solution for 9 and 12 infiltrations and the reference sample in both dry and humidified H_2 (50% H_2 :50% H_2O) at a temperature of 600 °C. The 12 C infiltrated sample show a power density of $0.53 \text{ W} \cdot \text{cm}^{-2}$ at 600 °C, an increase of 8% over the reference sample. Fuel mode measurements also showed an increase in current density at the same potential for the 12 C LSC

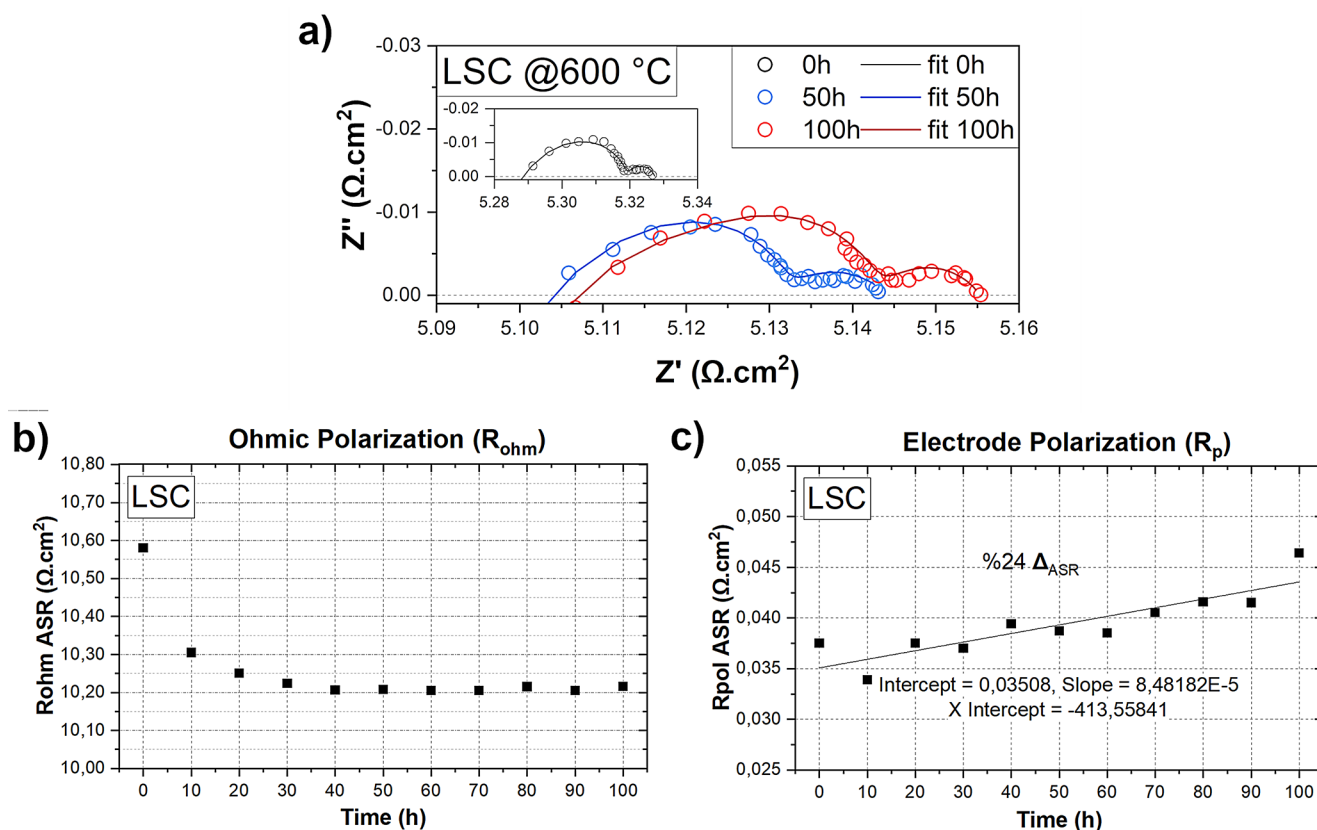


Fig. 7 Long-term ASR values of a) R_{ohm} and c) R_p of LSC at 600 °C

infiltrated sample compared to the reference. The increase was analyzed using the potential of 0.7 V, which yielded a value of $0.62 \text{ A} \cdot \text{cm}^{-2}$ to $0.7 \text{ A} \cdot \text{cm}^{-2}$ for the reference sample and 12 C LSC, respectively. Furthermore, a lower slope was observed in the electrolysis mode, confirming the trend above. This observation indicates an increase in the electrochemical activity of the cell. It has been shown that due to the identical fuel electrode and electrolyte, the obtained increase in power density was related to the increased electrochemical efficiency of the oxygen electrode. At the same time, a reduction in the polarization resistance of the cell was observed for both dry and wet hydrogen. In the case of dry hydrogen, R_p was $1.8 \Omega \cdot \text{cm}^2$ compared to $2.3 \Omega \cdot \text{cm}^2$ for the reference sample, a reduction of approximately 22% compared to the reference sample. A similar relationship occurs in the case of wet hydrogen where the R_p for the 12 C LSC impregnated sample was $0.47 \Omega \cdot \text{cm}^2$ compared to $0.55 \Omega \cdot \text{cm}^2$ for the reference sample, a reduction of approximately 15%.

4 Discussion and literature comparison

4.1 Symmetrical cells

To facilitate a more comprehensive interpretation of the results, a comparative analysis was conducted to identify any potential discrepancies between the findings and the existing literature. In the present study, the oxygen electrode formed of a porous backbone of GDC immersed in LSC exhibited the most promising electrochemical performance. The polarization resistance was observed to be $0.029 \Omega \cdot \text{cm}^2$ and $7.89 \Omega \cdot \text{cm}^2$ at 600 °C and 400 °C, respectively. The LSC: PrOx composite infiltration exhibits an intermediate performance compared to single phase compositions, with R_p values of $0.23 \Omega \cdot \text{cm}^2$ and $9.75 \Omega \cdot \text{cm}^2$ at 600 °C and 400 °C, respectively. The highest R_p values were observed for samples immersed in PrOx alone, with polarization resistance at 600 °C and 400 °C being $0.42 \Omega \cdot \text{cm}^2$ and $17.38 \Omega \cdot \text{cm}^2$, respectively.

In a similar study, A. Samson et al. examined the infiltration of the same composition (LSC64) into a screen-printed porous GDC backbone on a sintered GDC electrolyte at 1050 °C. They observed a polarization resistance of $0.044 \Omega \cdot \text{cm}^2$ and $6.04 \Omega \cdot \text{cm}^2$ at 600 °C and 400 °C respectively. Despite the use of a very thin electrolyte (180 μm), an

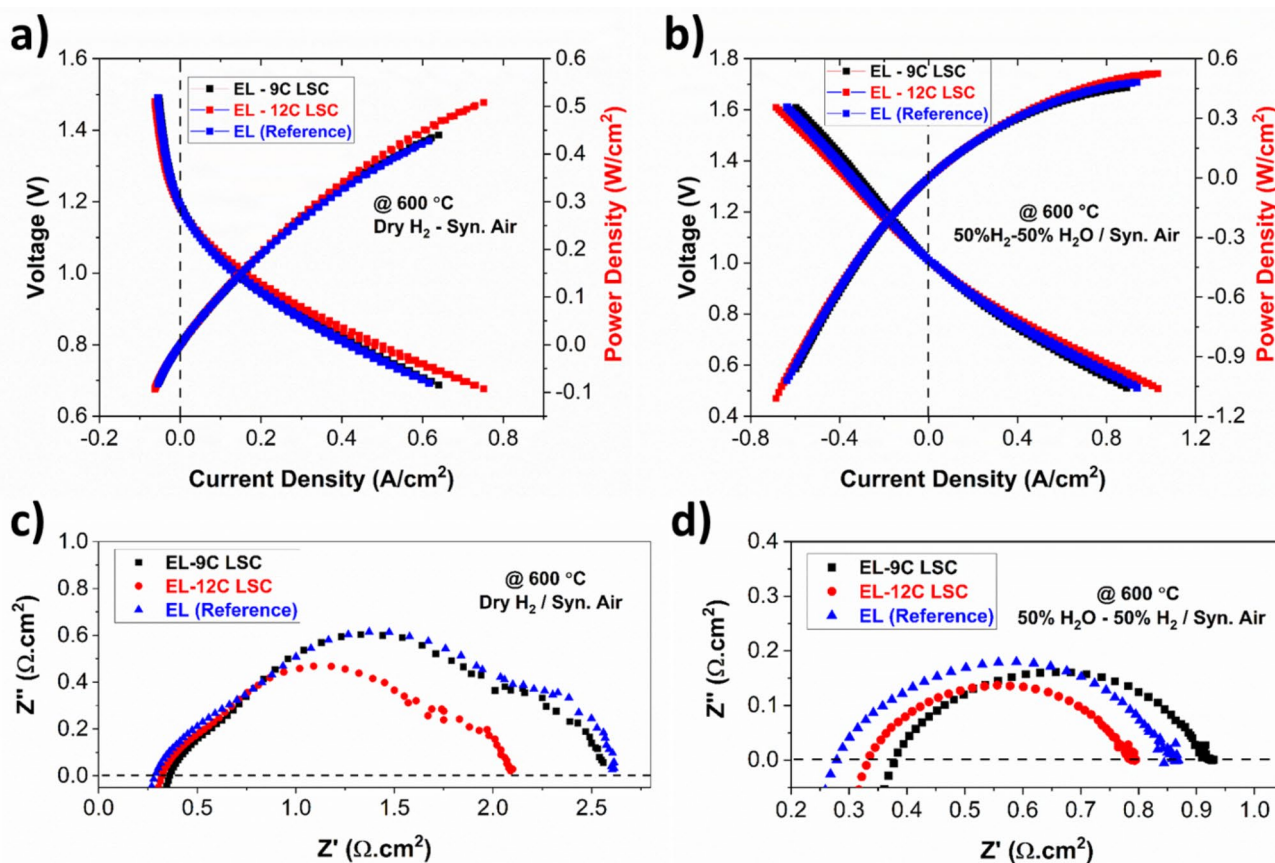


Fig. 8 Power, I-V curve and EIS data of infiltrated commercial fuel cells in dry (a, c), and 50% humidified fuel conditions (b, d)

infiltration loading of 9 times that used in this study, and a polymeric precursor concentration of 1 M, which is 5 times higher than that used in this study [34]. In the latter work, the same group achieved a value of $0.062 \Omega \cdot \text{cm}^2$ with the six cycles of infiltration of the LSC [42]. Ovtar S. et al. achieved a R_p value of $0.031 \Omega \cdot \text{cm}^2$ at a temperature of 700°C . The electrode was produced through a process of infiltration, whereby a YSZ backbone was subjected to six layers of GDC and subsequently nine layers of LSC [44]. In the work of Zhao Fei et al., the infiltration of LSC into samaria-doped ceria (SDC, $\text{Sm}_{0.2}\text{Ce}_{0.8}\text{O}_{2-\delta}$) backbone onto SDC electrolyte has been conducted, resulting in an R_p of $0.281 \Omega \cdot \text{cm}^2$ after subjecting the material to various thermal cycling regimes [45]. In a study conducted by Chrzan A. et al., symmetrical cells infiltrated with $\text{La}_{0.6}\text{Sr}_{0.4}\text{Co}_{0.2}\text{Fe}_{0.8}\text{O}_{3-\delta}$ were prepared. The objective was to investigate the effects of sintering temperature, thickness of the backbone and electrolyte, and the number of infiltration cycles on the polarization resistance. Additionally, the molarity of the infiltration solution was varied. At 600°C , the polarization resistance achieved was $0.16 \Omega \cdot \text{cm}^2$. The inferior performance observed in this study may be attributed to the use of coarser GDC particles, which result in diminished electrocatalytic activity due to the shortened TPB and reduced active area [46].

Nicollet C et al. conducted an infiltration process of Pr_6O_{11} into screen-printed $10 \mu\text{m}$ $\text{LaNi}_{0.6}\text{Fe}_{0.4}\text{O}_{3-\delta}$ (LNF) or GDC backbone ($7\text{--}14 \mu\text{m}$) onto a commercially available $100 \mu\text{m}$ 3% YSZ dense electrolyte. Notably, the polarization resistance was found to be $0.028 \Omega \cdot \text{cm}^2$ at 600°C . The molar concentration of Pr nitrate was 2 M, which is tenfold higher than that used in our work [18]. In a recent study, Caizán-Juanarena et al. investigated the potential of Pr_6O_{11} -infiltrated LSM-GDC backbone prepared by spray pyrolysis as an efficient oxygen electrode for solid oxide fuel cells. Electrochemical impedance spectroscopy measurements revealed a polarization resistance of $0.3 \Omega \cdot \text{cm}^2$ and $44.5 \Omega \cdot \text{cm}^2 R_{\text{ohm}}$ at 650°C [47]. In our work, $22.84 \Omega \cdot \text{cm}^2$ of R_{ohm} was obtained for samples infiltrated with PrOx itself at 600°C .

The values obtained for the sample immersed in PrOx: LSC composite exhibit a higher polarization resistance than those reported by Xiaofeng T. et al. for Pr-doped GDC (CGPO) and LSC, which is not a composite mixture, but a comparison in terms of Pr involvement may be reasonable. The composite mixture was infiltrated twice with CGPO and nine times with LSC into the GDC backbone, resulting in an R_p of $0.104 \Omega \cdot \text{cm}^2$ at 700°C [48].

4.2 Full cells

As previously stated, the infiltration of oxygen electrodes has been identified as a popular method for enhancing cell performance in the literature. However, the majority of these studies reported the performance of cells measured above 700 °C [44, 49–56]. The utilisation of anode-supported solid oxide cells at such low temperatures remains a relatively uncommon practice, although this operating temperature is gaining in popularity. For example, Samson A.C. et al. reported 1.28 $\Omega\cdot\text{cm}^2$ total polarization of a similar cell with an LSC-infiltrated GDC oxygen electrode at 650 °C [57]. The anode was fueled by humidified H_2 (80% H_2 :20% H_2O). In another study with a similar cell structure, Rehman S.U. et al. showed that infiltrating LSC into a porous GDC decreased the total polarization from 2.11 $\Omega\cdot\text{cm}^2$ to 1.32 $\Omega\cdot\text{cm}^2$ when compared to the conventionally fabricated LSC-GDC oxygen electrode [58]. The study reported an increase in power density from 0.48 $\text{W}\cdot\text{cm}^{-2}$ to 0.82 $\text{W}\cdot\text{cm}^{-2}$. The measurements were carried out at 650 °C with dry H_2 as fuel. Huang et al. studied LSC infiltration into an LSCF-SDC cathode integrated with a Ni-GDC anode-supported GDC electrolyte cell and claimed maximum power densities of 0.8 and 0.4 $\text{W}\cdot\text{cm}^{-2}$ at 600 and 550 °C, respectively [59]. In this current study, similar to the literature, a trend to increase performance with the infiltration method was demonstrated, and a power density of 0.53 $\text{W}\cdot\text{cm}^{-2}$ was obtained at 600 °C.

5 Conclusion

Infiltration process of LSC, LSC: PrOx and PrOx into the porous backbone GDC was prepared with wet powder spraying, as an porous oxygen electrode for intermediate solid oxide cells. It was found that an effective infiltration process was carried out by the immersion method. SEM-EDX analysis showed a uniform distribution of the immerse material in the porous backbone, both on the surface and in the electrolyte. In addition, the LSC infiltration was shown to be more effective than the PrOx infiltration.

Electrochemical impedance spectroscopy measurements showed a very low value of polarization resistance for LSC-immersed samples (0.029 $\Omega\cdot\text{cm}^2$ at 600 °C). Specimens infiltrated with the LSC: PrOx composite showed intermediate values (0.23 $\Omega\cdot\text{cm}^2$ at the same temperature), and the worst results were obtained with samples infiltrated with only PrOx (0.42 $\Omega\cdot\text{cm}^2$ at the same temperature°C).

Long-term stability measurements showed a slight increase in the polarization resistance of the LSC-immersed sample. This value changed by 24% in 100 h. A decrease and stabilization of the ohmic resistance was also observed.

Measurements of full cells showed a high power density of 0.53 $\text{W}\cdot\text{cm}^{-2}$ at a temperature of 600 °C, an increase of 8% compared to the reference sample. Improvement was also demonstrated in all cell operating modes, both fuel and electrolyser. EIS measurements performed on the cells showed a reduction in polarization resistance for the LSC-infiltrated samples compared to the reference.

Acknowledgements This research has been supported by National Science Centre (NCN) DAINA 2 project number UMO-2020/38/L/ST8/00513: “Porous metal supported micro-scale solid oxide fuel cells: fundamentals, fabrication and testing”.

Authors contribution Ömer Faruk Aksoy - Writing – original draft, Writing - review & editing, Validation, Methodology, Investigation (Sample preparation, symmetrical cells measurements), Formal analysis, Data curation. Bartłomiej Lemieszek: Writing – original draft, Writing - review & editing, Validation, Methodology, Investigation (symmetrical cells measurements), Formal analysis, Data curation. Murat Murutoğlu – Writing - review & editing, Methodology, Investigation (Full cells measurements), Formal analysis, Data curation. Jakub Karczewski - Writing – review & editing, Methodology, Investigation. Piotr Jasiński - Writing – review & editing, Methodology. Sebastian Molin - Writing – review & editing, Supervision, Funding acquisition, Methodology, Conceptualization.

Data availability The raw/processed data from this study will be available on request from the corresponding author.

Declarations

Competing interests The authors declare that they have no known competing financial interests or personal relationships that could have appeared to influence the work reported in this paper.

Open Access This article is licensed under a Creative Commons Attribution 4.0 International License, which permits use, sharing, adaptation, distribution and reproduction in any medium or format, as long as you give appropriate credit to the original author(s) and the source, provide a link to the Creative Commons licence, and indicate if changes were made. The images or other third party material in this article are included in the article's Creative Commons licence, unless indicated otherwise in a credit line to the material. If material is not included in the article's Creative Commons licence and your intended use is not permitted by statutory regulation or exceeds the permitted use, you will need to obtain permission directly from the copyright holder. To view a copy of this licence, visit <http://creativecommons.org/licenses/by/4.0/>.

References

1. A. Alaswad, A. Baroutaji, A. Rezk, M. Ramadan, A.G. Olabi, *Advances in Solid Oxide Fuel Cell Materials. In Encyclopedia of Smart Materials*, pp. 334–340 (2020). <https://doi.org/10.1016/B978-0-12-803581-8.11743-6>
2. M. Ghamarinia, A. Babaei, C. Zamani, H. Aslannejad, Application of the distribution of relaxation time method in electrochemical analysis of the air electrodes in the SOFC/SOEC devices: a review. *Chem. Eng. J. Adv.* **15**, 100503 (2023). <https://doi.org/10.1016/J.CEJA.2023.100503>

3. A. Tarancón, Strategies for lowering solid oxide fuel cells operating temperature. *Energies*. **2**(4), 1130–1150 (2009). <https://doi.org/10.3390/en20401130>
4. J.C.W. Mah, A. Muchtar, M.R. Somalu, M.J. Ghazali, Metallic interconnects for solid oxide fuel cell: a review on protective coating and deposition techniques. *Int. J. Hydrogen Energy*. **42**(14), 9219–9229 (2017). <https://doi.org/10.1016/j.ijhydene.2016.03.195>
5. S. Chen, H. Zhang, C. Yao et al., Review of SOFC Cathode performance enhancement by surface modifications: recent advances and future directions. *Energy Fuels*. **37**(5), 3470–3487 (2023). <https://doi.org/10.1021/acs.energyfuels.2c03934>
6. B. Kamecki, G. Cempura, P. Jasiński, S.-F. Wang, S. Molin, Tuning Electrochemical performance by Microstructural Optimization of the Nanocrystalline Functional Oxygen Electrode Layer for Solid Oxide cells. *ACS Appl. Mater. Interfaces*. **14**(51), 57449–57459 (2022). <https://doi.org/10.1021/acsami.2c18951>
7. Z. Wang, X. Wang, Z. Xu et al., Semiconductor-ionic nanocomposite La_{0.1}Sr_{0.9}MnO_{3-δ}-CeO_{3-δ} functional layer for high performance low temperature SOFC. *Mater. (Basel)*. **11**(9) (2018). <https://doi.org/10.3390/MA11091549>
8. Z. Li, M. Li, Z. Zhu, Perovskite Cathode materials for low-temperature solid oxide fuel cells: fundamentals to optimization STO SrTiO₃ TEM transmission electron microscopy YSZ Yttria-stabilized zirconia. *1918*;5:263–311. <https://doi.org/10.1007/s41918-021-00098-3>
9. A. Evans, J. Martynczuk, D. Stender, C.W. Schneider, T. Lippert, M. Prestat, Low-temperature micro-solid oxide fuel cells with partially amorphous La_{0.6}Sr_{0.4}CoO_{3-δ} cathodes. *Adv. Energy Mater.* **5**(1), 1–9 (2015). <https://doi.org/10.1002/aenm.201400747>
10. B. Kamecki, J. Karczewski, H. Abdioli et al., Deposition and Electrical and Structural properties of La_{0.6}Sr_{0.4}CoO₃ thin films for Application in High-Temperature Electrochemical cells. *J. Electron. Mater.* **48**(9), 5428–5441 (2019). <https://doi.org/10.1007/s11664-019-07372-7>
11. J. Hayd, L. Dieterle, U. Guntow, D. Gerthsen, E. Ivers-Tiffée, Nanoscaled La_{0.6}Sr_{0.4}CoO_{3-δ} as intermediate temperature solid oxide fuel cell cathode: microstructure and electrochemical performance. *J. Power Sources*. **196**(17), 7263–7270 (2011). <https://doi.org/10.1016/J.JPOWSOUR.2010.11.147>
12. C. Kim, H. Lee, I. Jang et al., Subcontinuous 2D La_{0.6}Sr_{0.4}CoO_{3-δ} nanosheet as an efficient charge conductor for boosting the cathodic activity of solid oxide fuel cells. *Electrochim. Acta*. **366**, 137371 (2021). <https://doi.org/10.1016/J.ELECTACTA.2020.137371>
13. Y.T. Kim, N. Shikazono, Investigation of La_{0.6}Sr_{0.4}CoO_{3-δ}-Gd_{0.1}Ce_{0.9}O_{2-δ} composite cathodes with different volume ratios by three-dimensional reconstruction. *Solid State Ionics*. **309**, 77–85 (2017). <https://doi.org/10.1016/J.SSI.2017.07.010>
14. Y.J. Jin, Z.G. Liu, Z.Y. Ding, G. Cao, J.H. Ouyang, Preparation, microstructure and electrical property of GdSmZr₂O₇-(Li_{0.52}Na_{0.48})₂CO₃ composite electrolyte via carbonate infiltration. *Ceram. Int.* **46**(5), 5689–5694 (2020). <https://doi.org/10.1016/J.CERAMINT.2019.11.016>
15. Y.T. Kim, A. Ohi, A. He et al., Microstructure and polarization characteristics of LSCF-GDC composite cathode with different volume fractions. *ECS Trans.* **68**(1), 757–762 (2015). <https://doi.org/10.1149/06801.0757ecst>
16. A. Donazzi, G. Cordaro, A. Baricci, Z. Ding, M. Bin, Maestri, A detailed kinetic model for the reduction of oxygen on LSCF-GDC composite cathodes. *Electrochim. Acta*. **335**, 135620 (2020). <https://doi.org/10.1016/J.ELECTACTA.2020.135620>
17. C. Fu, K. Sun, N. Zhang, X. Chen, D. Zhou, Electrochemical characteristics of LSCF-SDC composite cathode for intermediate temperature SOFC. *Electrochim. Acta*. **52**(13), 4589–4594 (2007). <https://doi.org/10.1016/J.ELECTACTA.2007.01.001>
18. C. Nicollet, A. Flura, V. Vibhu, A. Rougier, J.M. Bassat, J.C. Grenier, An innovative efficient oxygen electrode for SOFC: Pr₆O₁₁ infiltrated into Gd-doped ceria backbone. *Int. J. Hydrogen Energy*. **41**(34), 15538–15544 (2016). <https://doi.org/10.1016/j.ijhydene.2016.04.024>
19. L. Yefsah, J. Laurencin, M. Hubert et al., Electrochemical performance and stability of PrO_{1.833} as an oxygen electrode for solid oxide electrolysis cells. *Solid State Ionics*. **399**(March), 1–14 (2023). <https://doi.org/10.1016/j.ssi.2023.116316>
20. M.R. Somalu, A. Muchtar, W.R.W. Daud, N.P. Brandon, Screen-printing inks for the fabrication of solid oxide fuel cell films: a review. *Renew. Sustain. Energy Rev.* **75**(December 2015), 426–439 (2017). <https://doi.org/10.1016/j.rser.2016.11.008>
21. H. Zhang, T. Chen, Z. Huang, G. Hu, J. Zhou, S. Wang, A cathode-supported solid oxide fuel cell prepared by the phase-inversion tape casting and impregnating method. *Int. J. Hydrogen Energy*. **47**(43), 18810–18819 (2022). <https://doi.org/10.1016/j.ijhydene.2022.04.021>
22. J.H. Myung, H.J. Ko, H.G. Park, M. Hwan, S.H. Hyun, Fabrication and characterization of planar-type SOFC unit cells using the tape-casting/lamination/co-firing method. *Int. J. Hydrogen Energy*. **37**(1), 498–504 (2012). <https://doi.org/10.1016/J.IJHYDENE.2011.09.011>
23. C. Yuan, Y. Liu, Y. Zhou, Z. Zhan, S. Wang, Fabrication and characterization of a cathode-support solid oxide fuel cell by tape casting and lamination. *Int. J. Hydrogen Energy*. **38**(36), 16584–16589 (2013). <https://doi.org/10.1016/J.IJHYDENE.2013.08.146>
24. S. Zhang, L. Bi, L. Zhang, C. Yang, H. Wang, W. Liu, Fabrication of cathode supported solid oxide fuel cell by multi-layer tape casting and co-firing method. *Int. J. Hydrogen Energy*. **34**(18), 7789–7794 (2009). <https://doi.org/10.1016/J.IJHYDENE.2009.07.081>
25. A. Evans, C. Benel, A.J. Darbandi et al., Integration of spin-coated nanoparticulate-based La_{0.6}Sr_{0.4}CoO_{3-δ} cathodes into micro-solid oxide fuel cell membranes. *Fuel Cells*. **13**(3), 441–444 (2013). <https://doi.org/10.1002/fuce.201300020>
26. Z. Wang, W. Weng, K. Chen, G. Shen, P. Du, G. Han, Preparation and performance of nanostructured porous thin cathode for low-temperature solid oxide fuel cells by spin-coating method. *J. Power Sources*. **175**(1), 430–435 (2008). <https://doi.org/10.1016/J.JPOWSOUR.2007.09.092>
27. B. Lemieszek, M. Ilickas, J. Jamroz et al., Enhanced electrochemical performance of partially amorphous La_{0.6}Sr_{0.4}CoO_{3-δ} oxygen electrode materials for low-temperature solid oxide cells operating at 400°C. *Appl. Surf. Sci.* **670** (2024). <https://doi.org/10.1016/j.apsusc.2024.160620>
28. L. Baqué, A. Serquis, Microstructural characterization of La_{0.4}Sr_{0.6}Co_{0.8}Fe_{0.2}O_{3-δ} films deposited by dip coating. *Appl. Surf. Sci.* **254**(1), 213–218 (2007). (SPEC. ISS.). <https://doi.org/10.1016/j.apsusc.2007.07.033>
29. M. Xu, J. Yu, Y. Song, R. Ran, W. Wang, Z. Shao, Advances in Ceramic Thin films fabricated by Pulsed Laser Deposition for Intermediate-Temperature Solid Oxide fuel cells. *Energy Fuels*. **34**(9), 10568–10582 (2020). <https://doi.org/10.1021/acs.energyfuels.0c02338>
30. Y. Chen, L. Liang, S.A. Paredes Navia, A. Hinerman, K. Gerdes, X. Song, Synergetic Interaction of Additive Dual nanocatalysts to accelerate Oxygen reduction reaction in fuel cell cathodes. *ACS Catal.* **9**(8), 6664–6671 (2019). <https://doi.org/10.1021/acscatal.9b00811>
31. A. Seong, J. Kim, O. Kwon et al., Self-reconstructed interlayer derived by in-situ mn diffusion from La_{0.5}Sr_{0.5}MnO₃ via atomic layer deposition for an efficient bi-functional electrocatalyst. *Nano Energy*. **71**(January), 104564 (2020). <https://doi.org/10.1016/j.nanoen.2020.104564>
32. C. Xiong, S. Xu, X. Li et al., Surface regulating and hetero-interface engineering of an LSCF cathode by CVD for solid oxide fuel

- cells: integration of improved electrochemical performance and Cr-tolerance. *J. Mater. Chem. A* **11**(29), 15760–15768 (2023). <https://doi.org/10.1039/d3ta02249h>
33. F.L.W.C. Jung, F.L.J.J. Kim, F.L.H.L. Tuller, Investigation of nanoporous platinum thin films fabricated by reactive sputtering: application as micro-SOFC electrode. *J. Power Sources*. **275**, 860–865 (2015). <https://doi.org/10.1016/j.jpowsour.2014.11.084>
 34. A. Samson, M. Søgaard, R. Knibbe, N. Bonanos, High performance cathodes for solid oxide fuel cells prepared by infiltration of $\text{La}_{0.6}\text{Sr}_{0.4}\text{CoO}_{3-\delta}$ into Gd-Doped Ceria. *J. Electrochem. Soc.* **158**(6), B650 (2011). <https://doi.org/10.1149/1.3571249>
 35. R. Zeng, Y. Huang, Enhancing surface activity of $\text{La}_{0.6}\text{Sr}_{0.4}\text{CoO}_{3-\delta}$ cathode by a simple infiltration process. *Int. J. Hydrogen Energy*. **42**(10), 7220–7225 (2017). <https://doi.org/10.1016/j.ijhydene.2016.04.014>
 36. D. Ding, M. Liu, M. Liu, S.O.F.C. Enhancing, Electrode Performance through Surface Modification. *ECS Trans.* **57**(1), 1801–1810 (2013). <https://doi.org/10.1149/05701.1801ecst>
 37. S. Choi, S. Yoo, J. Shin, G. Kim, J.E. Soc, B-b P. High Performance SOFC Cathode prepared by infiltration of $\text{La}_{n+1}\text{Ni}_n\text{O}_{3n+1}$ ($n=1, 2$, and 3) in porous YSZ High Performance SOFC Cathode prepared by infiltration. *J. Electrochem. Soc.* **158**(8), B995–B999 (2011). <https://doi.org/10.1149/1.3598170>
 38. M. Shah, S.A. Barnett, Solid oxide fuel cell cathodes by infiltration of $\text{La}_{0.6}\text{Sr}_{0.4}\text{Co}_{0.2}\text{Fe}_{0.8}\text{O}_{3-\delta}$ into Gd-Doped Ceria. *Solid State Ionics*. **179**(35–36), 2059–2064 (2008). <https://doi.org/10.1016/J.SSI.2008.07.002>
 39. Y. Huang, J.M. Vohs, R.J. Gorte, SOFC cathodes prepared by infiltration with various LSM precursors. *Electrochem. Solid-State Lett.* **9**(5), 237–240 (2006). <https://doi.org/10.1149/1.2183867>
 40. Y. Cheng, A.S. Yu, X. Li, T. Oh, J.M. Vohs, R.J. Gorte, Preparation of SOFC cathodes by infiltration into LSF-YSZ composite scaffolds. *J. Electrochem. Soc.* **163**(2), 54–58 (2016). <https://doi.org/10.1149/2.0171602jes>
 41. M.P. Pechini, Method of Preparing Lead and Alkalne Earth Titanates and Nobates and coating method using the same to form a Capacitor, *US Pat 3,330,697*. Published online 1967:2
 42. A.J. Samson, M. Sgaard, N. Bonanos, Electrodes for solid oxide fuel cells based on infiltration of co-based materials. *Electrochem. Solid-State Lett.* **15**(4), 54–56 (2012). <https://doi.org/10.1149/2.020204esl>
 43. V. Thangadurai, R.A. Huggins, W. Weppner, Mixed ionic-electronic conductivity in phases in the praseodymium oxide system. *J. Solid State Electrochem.* **5**, 531–537 (2001). <https://doi.org/10.1007/s100080000187>
 44. S. Ovtar, A. Hauch, S. Veltzé, M. Chen, Comparison between $\text{La}_{0.6}\text{Sr}_{0.4}\text{CoO}_{3-\delta}$ and $\text{LaNi}_{0.6}\text{Co}_{0.4}\text{O}_{3-\delta}$ infiltrated oxygen electrodes for long-term durable solid oxide fuel cells. *Electrochim. Acta*. **266**, 293–304 (2018). <https://doi.org/10.1016/j.electacta.2018.02.022>
 45. F. Zhao, R. Peng, C. Xia, A $\text{La}_{0.6}\text{Sr}_{0.4}\text{CoO}_{3-\delta}$ -based electrode with high durability for intermediate temperature solid oxide fuel cells. *Mater. Res. Bull.* **43**(2), 370–376 (2008). <https://doi.org/10.1016/j.materresbull.2007.03.006>
 46. A. Chrzan, J. Karczewski, M. Gazda, D. Szymczewska, P. Jasinski, $\text{La}_{0.6}\text{Sr}_{0.4}\text{Co}_{0.2}\text{Fe}_{0.8}\text{O}_{3-\delta}$ oxygen electrodes for solid oxide cells prepared by polymer precursor and nitrates solution infiltration into gadolinium doped ceria backbone. *J. Eur. Ceram. Soc.* **37**(11), 3559–3564 (2017). <https://doi.org/10.1016/j.jeurceramsoc.2017.04.032>
 47. L. Caizán-Juanarena, J. Zamudio-García, D. Marrero-López, Electrochemical investigation of Pr_6O_{11} infiltration into $\text{La}_{0.8}\text{Sr}_{0.2}\text{MnO}_{3-\delta}\text{-Ce}_{0.9}\text{Gd}_{0.1}\text{O}_{1.95}$ cathodes for IT-SOFC. *Ceram. Int.* **49**(21), 33717–33724 (2023). <https://doi.org/10.1016/j.ceramint.2023.08.060>
 48. X. Tong, C. Li, K. Xu et al., Nanoengineering of electrodes via infiltration: an opportunity for developing large-area solid oxide fuel cells with high power density. *Nanoscale*. **15**(40), 16362–16370 (2023). <https://doi.org/10.1039/d3nr02704j>
 49. H. Fan, M. Keane, N. Li, D. Tang, P. Singh, ScienceDirect infiltrated YSZ oxygen electrode for reversible solid oxide fuel cells. 2014;9. <https://doi.org/10.1016/j.ijhydene.2014.05.149>
 50. X. Tong, S. Ovtar, K. Brodersen, P.V. Hendriksen, M. Chen, A 4 × 4 cm 2 Nanoengineered Solid Oxide Electrolysis Cell for Efficient and Durable Hydrogen Production. Published online 2019. <https://doi.org/10.1021/acsami.9b07749>
 51. S. Ur, H. Song, H. Kim et al., A dynamic infiltration technique to synthesize nanolayered cathodes for high performance and robust solid oxide fuel cells. *J. Energy Chem.* **70**, 201–210 (2022). <https://doi.org/10.1016/j.ijechem.2022.02.052>
 52. Y. Namgung, J. Hong, A. Kumar, D.K. Lim, S.J. Song, One step infiltration induced multi-cation oxide nanocatalyst for load proof SOFC application. *Appl. Catal. B Environ.* **267**(November 2019), 118374 (2020). <https://doi.org/10.1016/j.apcatb.2019.118374>
 53. Song YH, Rehman SU, Kim HS et al., Facile surface modification of LSCF/GDC cathodes by epitaxial deposition of $\text{Sm}_{0.5}\text{Sr}_{0.5}\text{CoO}_3$ via ultrasonic spray infiltration. *J. Mater. Chem. A*. **8**(7), 3967–3977 (2020). <https://doi.org/10.1039/c9ta11704k>
 54. L. Sr, H. Ahmad, M. Zubair et al., ScienceDirect Boosting performance of the solid oxide fuel cell by. *Int. J. Hydrogen Energy*. **47**(88), 37587–37598 (2021). <https://doi.org/10.1016/j.ijhydene.2021.11.109>
 55. Z. Zheng, J. Jing, Z. Lei, Z. Wang, Z. Yang, ScienceDirect Performance and DRT analysis of infiltrated functional cathode based on the anode supported SOFCs with long-term stability. *Int. J. Hydrogen Energy*. **47**(41), 18139–18147 (2022). <https://doi.org/10.1016/j.ijhydene.2022.03.289>
 56. Samson AJ, Søgaard M, Hjalmarsson P et al., Durability and performance of high performance infiltration cathodes. **13**(4), 511–519 (2013). <https://doi.org/10.1002/fuce.201200183>
 57. A.J. Samson, P. Hjalmarsson, M. Søgaard, J. Hjelm, N. Bonanos, Highly durable anode supported solid oxide fuel cell with an infiltrated cathode. 2012;**216**:124–130. <https://doi.org/10.1016/j.jpowsour.2012.05.040>
 58. S. Ur, M. Haseeb, H. Kim et al., Applied Catalysis B: Environmental Designing the nano-scale architecture of the air electrode for high-performance and robust reversible solid oxide cells. *Appl. Catal. B Environ.* **333**(December 2022), 122784 (2023). <https://doi.org/10.1016/j.apcatb.2023.122784>
 59. Y. Huang, A.M. Hussain, E.D. Wachsman, Nano Energy Nanoscale cathode modification for high performance and stable low-temperature solid oxide fuel cells (SOFCs). *Nano Energy*. **49**(March), 186–192 (2018). <https://doi.org/10.1016/j.nanoen.2018.04.028>

Publisher's note Springer Nature remains neutral with regard to jurisdictional claims in published maps and institutional affiliations.